JOURNAL OF MATERIALS SCIENCE **35** (2000) 2643–2651

# Application of infrared imaging to the study of controlled failure of thermal barrier coatings*

M. K. FERBER, A. A. WERESZCZAK, M. LANCE, J. A. HAYNES
*Metals and Ceramics Division, Oak Ridge National Laboratory, Oak Ridge, TN 37831-6069, USA*
*E-mail: ferbermk@ornl.gov*

M. A. ANTELO
*GT Materials Development Department, Siemens Westinghouse Power Corporation, Orlando, FL 32826-2399, USA*

A technique that uses high resolution infrared (IR) imaging was developed to track and analyze damage evolution of thermal barrier coatings (TBCs) during controlled mechanical testing of a TBC specimen. Coating debonding and spallation were examined during a monotonic load-to-TBC-failure test. The infrared imaging, in concert with a controlled thermal gradient in the specimen, was particularly effective in identifying and tracking localized damage evolution because the damage in the TBC was always associated with a measurable surface-temperature change. It is demonstrated that the combined use of high-resolution infrared imaging and controlled mechanical testing of TBCs is an effective method to characterize the evolution of their failure. © *2000 Kluwer Academic Publishers*

## 1. Introduction

In 1992, the Department of Energy's Office of Industrial Technology initiated the Advanced Turbine Systems (ATS) Program with the primary objective of developing ultra high efficiency gas turbine systems for land-based utility and industrial markets. The utilization of thermal barrier coatings (TBCs) on various hot section components in the gas turbine has been identified as a major approach for achieving the higher turbine inlet temperatures associated with ATS performance goals. TBCs can be considered as a composite system consisting of a metal substrate, a ductile and oxidization-resistant metallic bond coat, and a thermally insulating ceramic top coat (traditionally zirconia with 8% yttria stabilizer). The top coat is deposited either by air plasma spraying (APS) or electron beam physical vapor deposition (EB-PVD).

A number of TBC systems have been successfully applied to aircraft engine applications with the expressed goal of life extension. Due to the conservative nature of the engine design conditions, coating failure in these applications can be tolerated without catastrophic loss of service function of the underlying metallic component. In the case of land-based turbines, the need for increased inlet temperatures and long operating lifetimes will necessitate highly reliable TBC systems. Thermal aging studies [1, 2] have shown that relatively short duration isothermal exposures to the proposed inlet temperatures cause significant microstructural changes. These changes result in higher thermal conductivities in the TBCs. An additional concern is the time (cycle) dependent failure which arises from the combined effects of thermal cycling, changes in thermal conductivity of the TBC-system constituents, and bond coat oxidation.

Previous studies [3–7] have attempted to quantify failure behavior through the measurement of coating-spallation-time (or cycles) as a function of thermal cycling. Failure is assumed to occur via a damage evolution mechanism that involves the generation of microcracks during the cooling portion of the thermal cycle. Because of the net thermal expansion mismatch between the ceramic coating and the bond-coat/substrate, the coating is subjected to tensile stresses during heating and compressive stresses during cooling. Coating spallation arises as microcracks coalesce to form larger macrocracks. Unfortunately the specific sequence of events associated with the spallation process are poorly understood.

Several spallation models [8, 9] assume that failure occurs as a result of buckling of the zirconia top coat during cooling. A major requirement of this model is the presence of a dominant microcrack at or near the zirconia top coat/bond coat interface. The crack supposedly grows under the influence of the stress intensity factor arising from the stress state during cooling. Contrary to this, a recent comprehensive microstructural analysis [10] of TBC specimens subjected to both isothermal aging and thermal cycling found limited evidence of

* Research supported by the U.S. Department of Energy, Assistant Secretary for Energy Efficiency and Renewable Energy, by two sources: (a) Office of Industrial Technologies, Advanced Turbine Systems Program, and (b) Office of Transportation Technologies, High Temperature Materials Laboratory Fellowship Program, both under contract DE-AC05-96OR22464 with Lockheed Martin Energy Research Corporation.

the buckling mechanism. In the case of the plasma-sprayed coatings examined in the study, the zirconia top coat became increasingly damaged with time as a result of localized microcracking. The application of piezospectroscopy to these samples [11] indicated that the compressive hydrostatic stresses supported by top coat also decreased (approached zero) with increases in the number of thermal cycles. The coating was less able to support stresses that arise during thermal cycling because of this damage. A simplified stress analysis suggested that the major role of the alumina scale that formed at the top coat-bond coat interface was to increase the localized tensile stresses thereby facilitating the microcracking process.

Existing models suggest that the number of cycles to failure (spallation) should be a power-law function of the inelastic strain change associated with a single thermal cycle [12, 13]. A limitation with this model is that the strain difference must be determined numerically. A further complication arises due to the fact that the stresses that develop upon cooling are also a function of the thickness of the alumina scale that forms on the bond coat during high-temperature oxidation. These stresses are also affected by time-dependent changes in the bond coat (resulting from creep and plastic deformation) and the zirconia top coat (arising from phase transformations and sintering).

A limited number of investigators [13–18] have attempted to mechanically simulate TBC failure resulting from thermal cycling. For example, DeMasi-Marcin, *et al*., [14] examined the damage generated in plasma-sprayed coatings machined from bulk deposits using four-point bending, uniaxial tension, and uniaxial compression tests. They attributed hysteresis in the tension-compression stress-strain behavior to a stick-slip mechanism involving shear-induced sliding of the opposing faces of microcracks. Although sliding was presumed to be reversible, the jagged nature of the crack faces led to energy dissipation (independent of the loading direction) and thus a hysteresis during load cycling. Unfortunately, the authors were unable to provide microstructural evidence for this mechanism.

The validations of the described TBC failure models have been limited by the lack of proven techniques to quantify the damage generated during mechanical and/or thermal loading. In a recent study [19], it was shown that the IR imaging had the potential to qualitatively measure this damage. In that study, an IR camera was used to map the surface temperatures of EB-PVD coated disks which had been previously subjected to thermal cycling (ramp to 1150°C with 1 hour hold at temperature). After cycling, each disk was placed on a hot plate in order to establish a modest temperature gradient through the thickness (Fig. 1). By assuming that the primary effect of thermal cycling was the generation of microcracks, changes in the average surface temperature could be directly related to the extent of this damage. As shown in Fig. 2, thermal cycling resulted in a drop in the average surface temperature consistent with the generation of microcracks within the thermally-grown alumina located between bond and top coats. In addition, for a given number of cycles, the surface temperature decreased significantly near the coating edges indicating that the damage was more extensive in these regions. Scanning electron microscopy confirmed that microcracking within the thermally-grown alumina scale was the primary damage mechanism.

The intent of this article is to provide a description of the coupled applicability of IR imaging and controlled mechanical testing to identify and quantify damage in

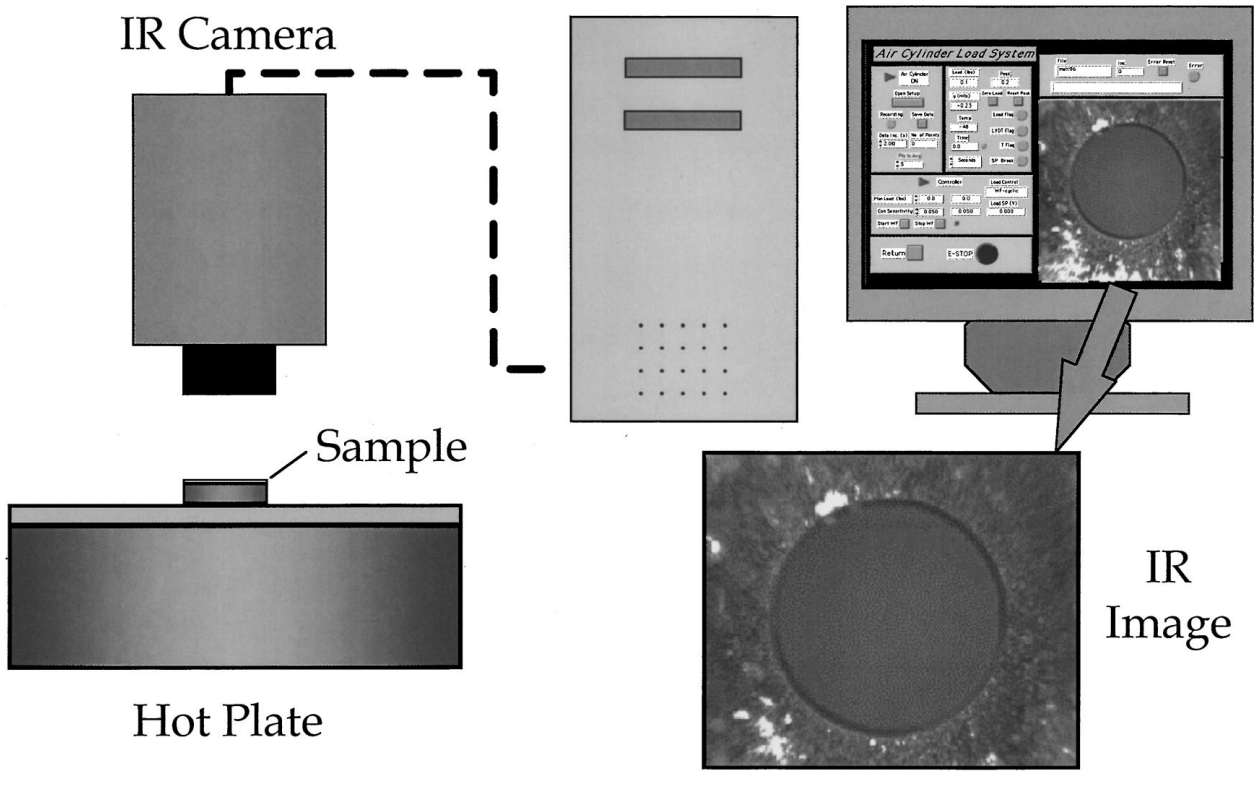


*Figure 1* An early motivation to the present study was provided by infrared imaging of thermally-excited TB-coated disks.

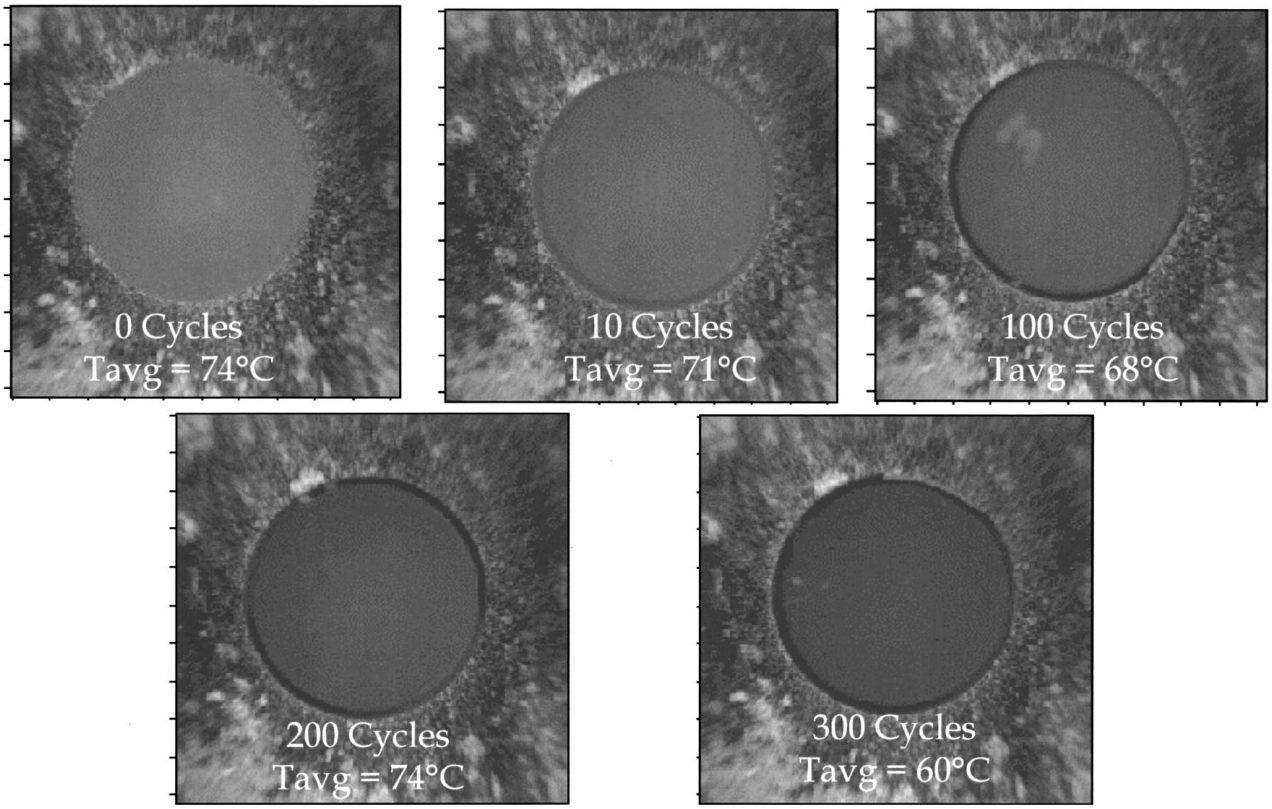


*Figure 2* Changes in surface temperature (and damage accumulation) as a function of thermal cycling were exploited with infrared imaging. Darker shading denotes a cooler temperature.

a TBC system. Room-temperature mechanical loading was selected over thermal cycling to eliminate time-temperature dependent mechanisms, isolating the mechanical tolerance aspect. A coated specimen was subjected to monotonic compression loading until coating spallation occurred. IR imaging was used with the direct imposition of a controlled thermal gradient in the specimen to identify and continuously monitor crack initiation (debonding) and coating spallation during its testing. Although characterizations of both APS and EB-PVD TBC systems have been performed by the authors, the examination of a spallation event in an APS TBC subjected to monotonic loading was the focus of the present study.

## 2. Experimental procedure

A cylindrical, hour-glass-shaped specimen was used for the TBC testing. The dimensions for the metal-substrate are shown in Fig. 3. A metal bond coat and APS zirconia top coat were deposited on its central length (including the specimen's 35 mm gage length). The 12.0 mm diameter shanks were not coated so to permit the direct gripping of the substrate.

An electromechanical test frame (Model 808, MTS, Eden Prairie, MN) was used for the uniaxial mechanical testing. The test specimens were mounted in hydraulic collet grips (646, MTS, Eden Prairie, MN). Prior to testing, a strain-gaged superalloy specimen was used in concert with a load-train-containing alignment fixture (MTS, Eden Prairie, MN) to minimize angular and concentric misalignment of the upper and lower hydraulic grips. Both misalignment types were adjusted to

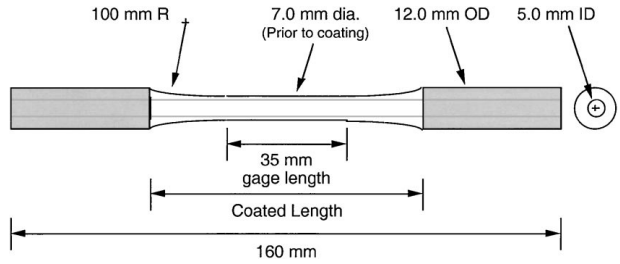


*Figure 3* Dimensions of coated test specimen.

be less than 2% at both compressive and tensile forces above 10 kN.

A contacting extensometer (Instron, Canton, MA) was used to monitor axial strain during the displacement-controlled load-to-coating-failure test.[†] Normally the extensometer with its capacitance gage has a resolution of $\approx\pm 0.025\ \mu$m ($\pm 10^{-6}$ mm/mm); however, because of environmental effects such as test-frame vibrations, electronic noise, etc., the effective extensometer resolution was approximately $\approx\pm 0.1\ \mu$m ($\pm 4 \times 10^{-6}$ mm/mm).[‡] The extensometer accuracy was calibrated and measured to be within $\pm 0.1\%$. Lastly, the

[†] For low cycle fatigue tests, this extensometer is used to control the cyclic strain application.

[‡] For LCF tests, the extensometer's control signal is tuned using the test frame's computer software's "auto-tuning" capability with a TBC-coated specimen. This tuning effort is very critical for the successful strain-controlled LCF testing of the coating because the strain that the extensometer measures is a consequence of strain transfer between the thin zirconia top coat, the thin metal bond coat and the relatively large (and stiff) superalloy substrate.

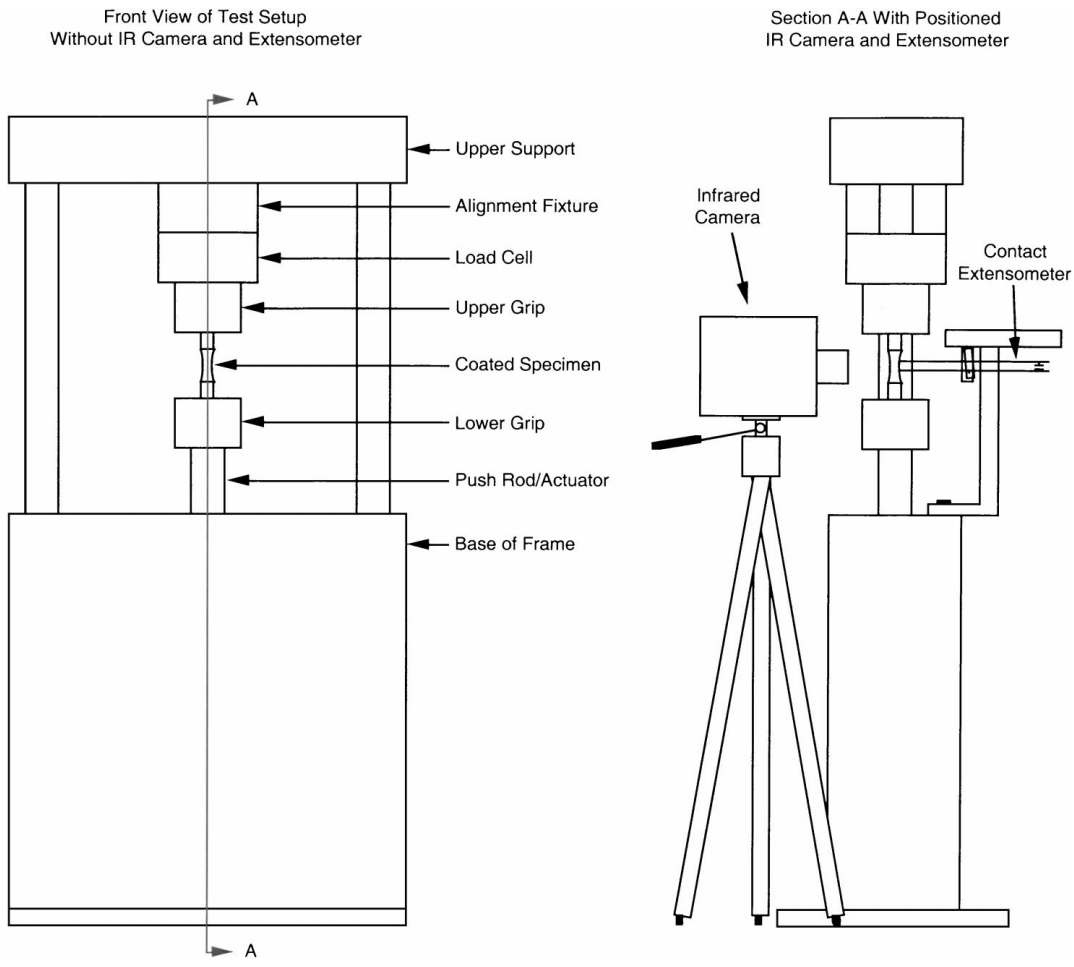


*Figure 4* Layout of the positioning of the infrared camera, test specimen, and extensometer.

horizontally applied extensometer force is adjustable and needed to be minimal (to avoid the inducement of crack initiation) while maintaining intimate contact with the APS coating during testing. The optimal extensometer force for this testing was approximately 0.2 N (30 g) per rod.

A high-resolution IR camera (Radiance 1t, Amber/Raytheon, Goleta, CA) with a 25 mm lens was used to map the temperature field of the APS top coat's surface during its mechanical loading. The camera contained a $256 \times 256$ pixel indium antimonide sensor that was sensitive in the 3–5 $\mu$m waveband. Each pixel represented $\approx 100\ \mu\text{m} \times 100\ \mu\text{m}$ projected area of the top coat surface and had a temperature resolution of $\approx \pm 0.1^{\circ}\text{C}$ throughout the examined temperature range.[§] The camera has a high speed (12 bit) video bus that was used to digitally capture the temperature distribution field as a function of time during the specimen's mechanical testing. A conventional VCR was also used to continuously videotape the camera's field of view.

The contact location between the coated specimen and extensometer was oriented to be diametrically opposed to the IR camera's field of view. A schematic of the IR camera, load frame, and extensometer positioning is illustrated in Fig. 4. Although there is a blind spot with this arrangement that is narrow and located on the extensometer side of the specimen, the evolution of coating spallation is usually visible through the field of view of the IR camera during the testing.

The detection of coating debonding required the establishment of a controlled thermal gradient through the specimen thickness. To promote this, the uncoated substrate shanks were heated with heating tape. A schematic showing a close-up view of this arrangement is shown in Fig. 5. The tape-heating of the shanks caused an effective internal heating of the specimen's gage section that further aided the identification of coating damage at the top coat's surface during mechanical testing because of the differing thermal conductivities of the substrate, bond coat, and top coat and the radial thermal gradient through them. For this case of a long cylindrical metallic rod (substrate) of length, $L$, maintained at a constant temperature, $T_{\text{i}}$, heat transfer ($q$) will occur radially through the top coat in accordance with the equation,

$$q = 2\pi L(T_{\text{i}} - T_{\text{a}}) \Big/ \left[ (1/k)\, \ln(r_{\text{o}}/r_{\text{i}}) + \frac{1}{(hr_{\text{o}})} \right]$$
$$= 2\pi L(T_{\text{i}} - T_{\text{c}}) \Big/ \left[ \left( \frac{1}{k} \right) \ln \left( \frac{r_{\text{o}}}{r_{\text{i}}} \right) \right], \qquad (1)$$

where $T_{\text{a}}$ is the ambient temperature, $T_{\text{c}}$ is the surface temperature of the coating, $r_{\text{i}}$ is the radius of substrate, $r_{\text{o}}$ is the radius of the substrate plus coating, $k$ is the thermal conductivity of the coating, and $h$ is the coefficient

[§] Note that the piezocaloric effect is readily observed with this temperature resolution during LCF testing.

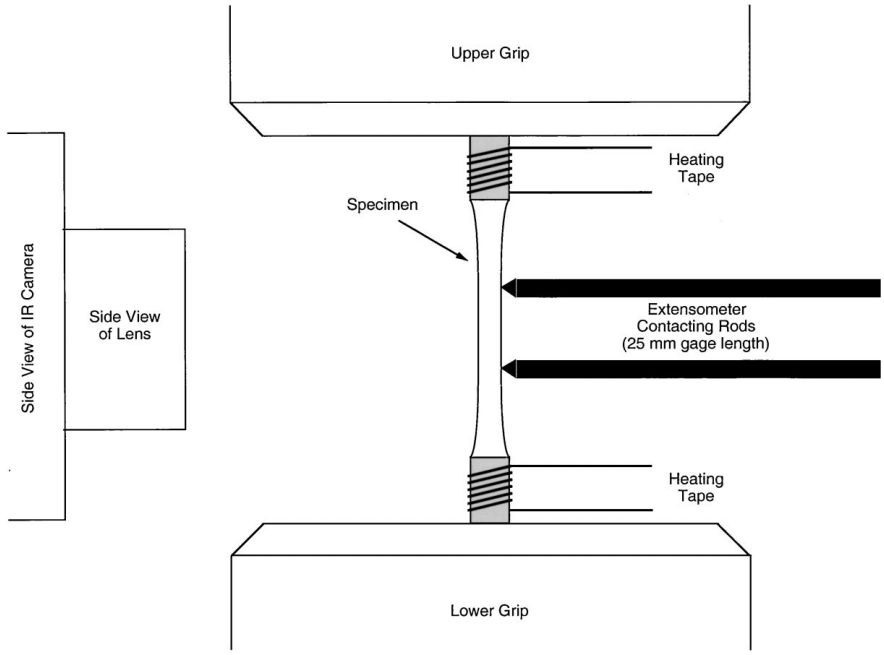


*Figure 5* Schematic showing a close-up view of the IR camera, test specimen, heating tape, and extensometer positioning.

of heat transfer from the coating surface to the surrounding environment. Preliminary calculations indicate that a 10% reduction in thermal conductivity should result in a coating surface decrease of at least 0.1°C, which is a change that is detectable with this IR camera. As a first approximation, the effect of microcracking on thermal conductivity can be described by the expression,

$$k_{\mathrm{m}} \cong k_{\mathrm{c}}\left[\frac{(1-v\mathrm{d})}{(1+v_{\mathrm{d}})}\right], \qquad (2)$$

where $k_{\mathrm{m}}$ is the effective thermal conductivity of the porous zirconia top coat, $k_{\mathrm{c}}$ is the thermal conductivity of dense zirconia, and $v_{\mathrm{d}}$ is the microcrack volume fraction. Equation 2 indicates that a small change in the microcrack density can significantly lower the effective thermal conductivity.

The described IR camera, coated specimen configuration, testing equipment and arrangement were used to produce a TBC failure in a monotonic test. The specimen was compressively loaded at a displacement


*Figure 6* Debonding and spallation are visible with the VCR image, but the resolution and imaging frequency are relatively limited.

rate of 0.75 $\mu$m/s until its coating spalled. The evolution of TBC failure using this IR monitoring technique and image analysis is illustrated.

## 3. Results

The IR image of the gripped (but unloaded) APS coated specimen after the temperatures generated with the heating tape had reached steady-state is illustrated in Fig. 6. The surface temperatures of the coating, which are represented by differing gray levels, ranged from 40 to 55°C (see shown scale). As expected, the application of the heating tape to the uncoated specimen ends resulted in a temperature gradient along the length of the specimen. In addition, two dark spots (indicated by the arrows in Fig. 6) were observed at the lower portion of the specimen. Three possible mechanisms can give rise to a difference in contrast on a IR image. First, if the coating were already debonded within these two regions, then the resulting reduction in the radial heat flow would lower surface temperatures in accordance with Equation 1 and produce a darker shade of gray. Such debonding is the cause for the dark band around the edge of the disk specimen subjected to 300 thermal cycles shown in Fig. 2. The second explanation is that contamination in the two regions may have locally decreased the emissivity due to deposits or contamination on the surface. Because the IR camera uses a constant emissivity to generate the temperature gray levels, the indicated temperatures in the two regions would be lower. The third cause of change in thermal contrast is the surface roughness. Protruding surfaces (eg. pits on EB-PVD coating) will appear darker since the same heat flux will have more area to diffuse. A careful visual examination of the specimen in the vicinity of the dark spots failed to reveal the presence of any foreign material and local surface irregularity.

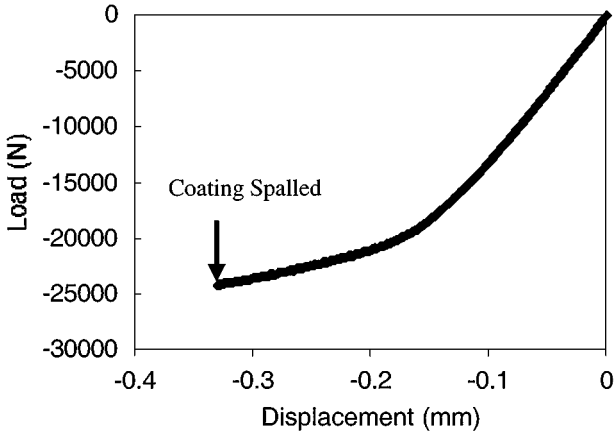


*Figure 7* The coating spalls at a compressive strain that exceeds the substrate's yield strain.

As shown by the load-displacement curve (Fig. 7), this spallation occurred well past the yield strain of the substrate. This observation is typical in these mechanical tests of TBCs; namely, the compressive strain that is required to initiate debonding and subsequent spallation generally exceeds the substrate's yield strain.

Selected IR images of the last 3 seconds of test extracted from the VCR tape are illustrated in Fig. 8. A coating spallation event (evident in the labeled "0 s" image) occurred at two locations within the gage section. They were easily detected since the removal of the coating exposed the underlying bond coat which being slightly warmer produced a lighter shade of gray in the IR image. Prior to spallation, debonding was observed at the lower portion of the specimen (indicated by the arrows in the "−1 s" image). Although there was some evidence that the debonding occurred well before this time, it was difficult to quantify its development or extent based solely on the visual output of the VCR.

To overcome the video analysis limitations associated with the VCR , the 12 bit video output from the IR camera was used for more detailed image analysis.

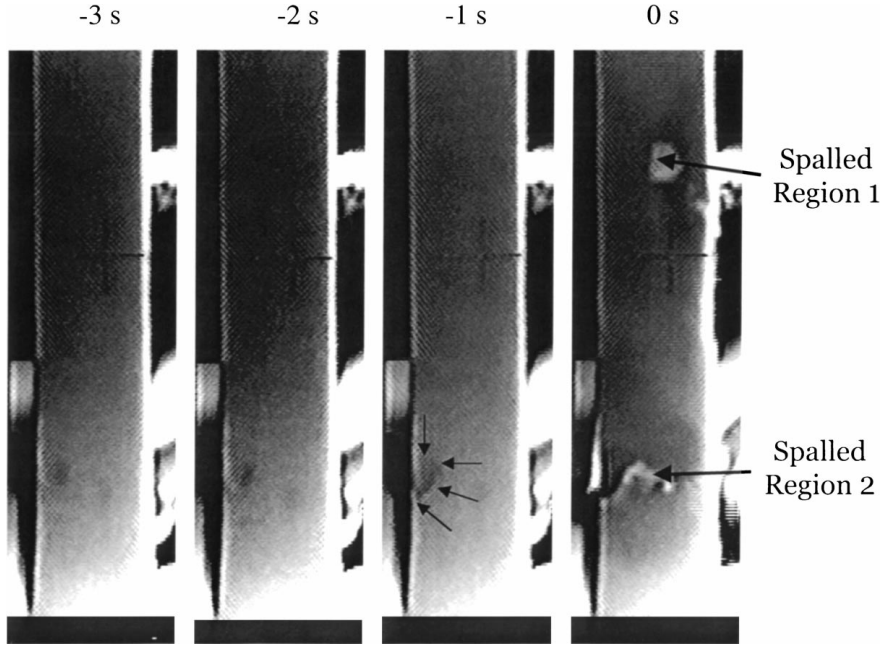


*Figure 8* Digitally-captured images allow more controllable tracking of the development of the spallation event.

Twelve-bit images were collected during testing at a rate of 10 frames/second and stored to disk as text files. These files were then analyzed using a software program written with LabVIEW™ 4.1 (National Instruments, Austin TX). As shown in Fig. 9, the series of captured images were first normalized by subtracting a reference image from them. The reference image in this case was taken at 3.5 seconds before spallation. The resulting processed image was very sensitive to identifying changes in temperature arising from the coating debonding. For example, a debonded region along the side of the specimen exploited by this reference-subtraction is shown in Fig. 9. The evolution of the debond region, which ultimately led to coating spallation in the lower portion of the specimen, is shown as a function of time in Fig. 10. Although the images in Fig. 10 did not reveal debonding in the vicinity of the upper region of spallation (Region 1), it is possible that

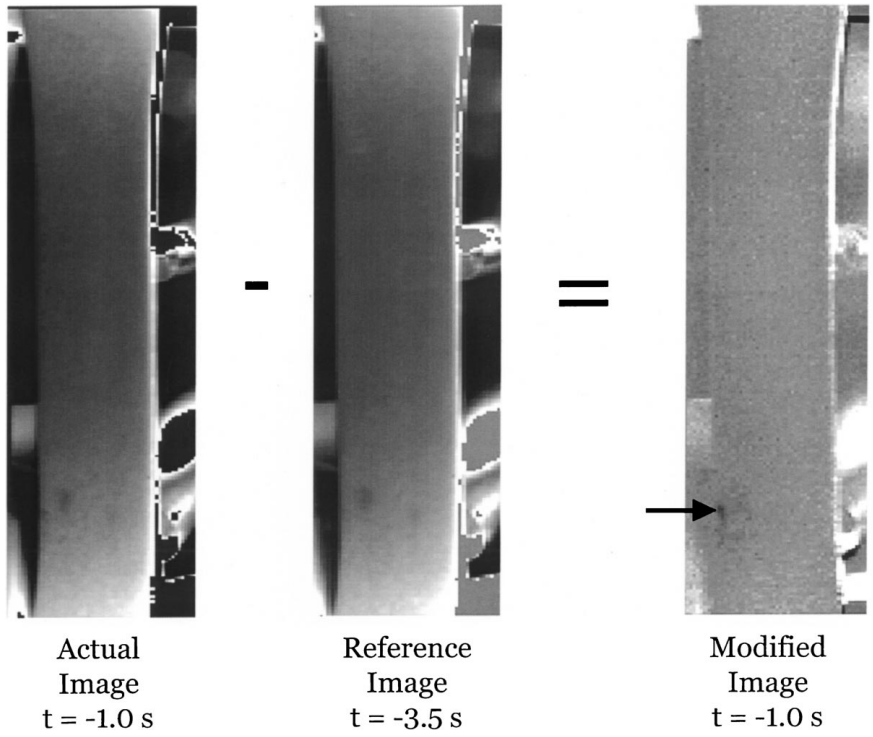


*Figure 9* The digital images may be analyzed to "subtract" off a reference state to more accurately sample surface temperature changes caused by damage.

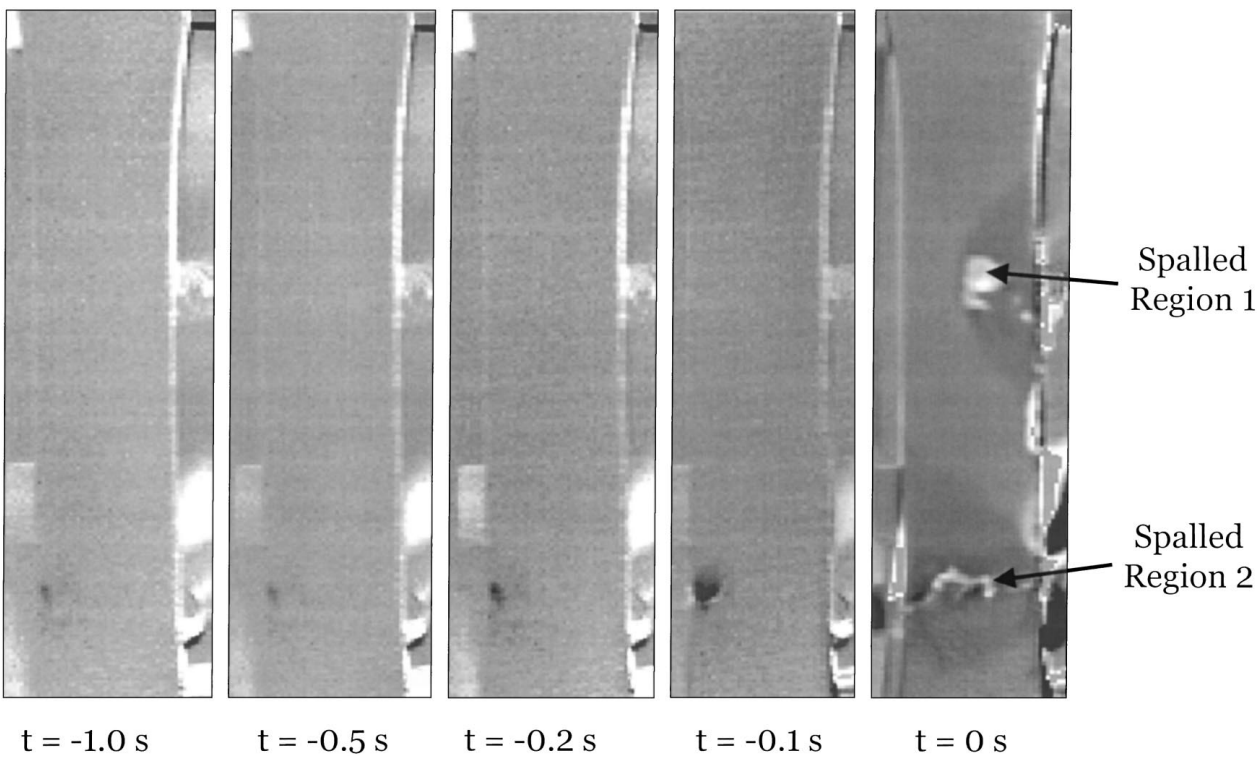


*Figure 10* Final one second showing the growth of the TBC debond and the spallation.

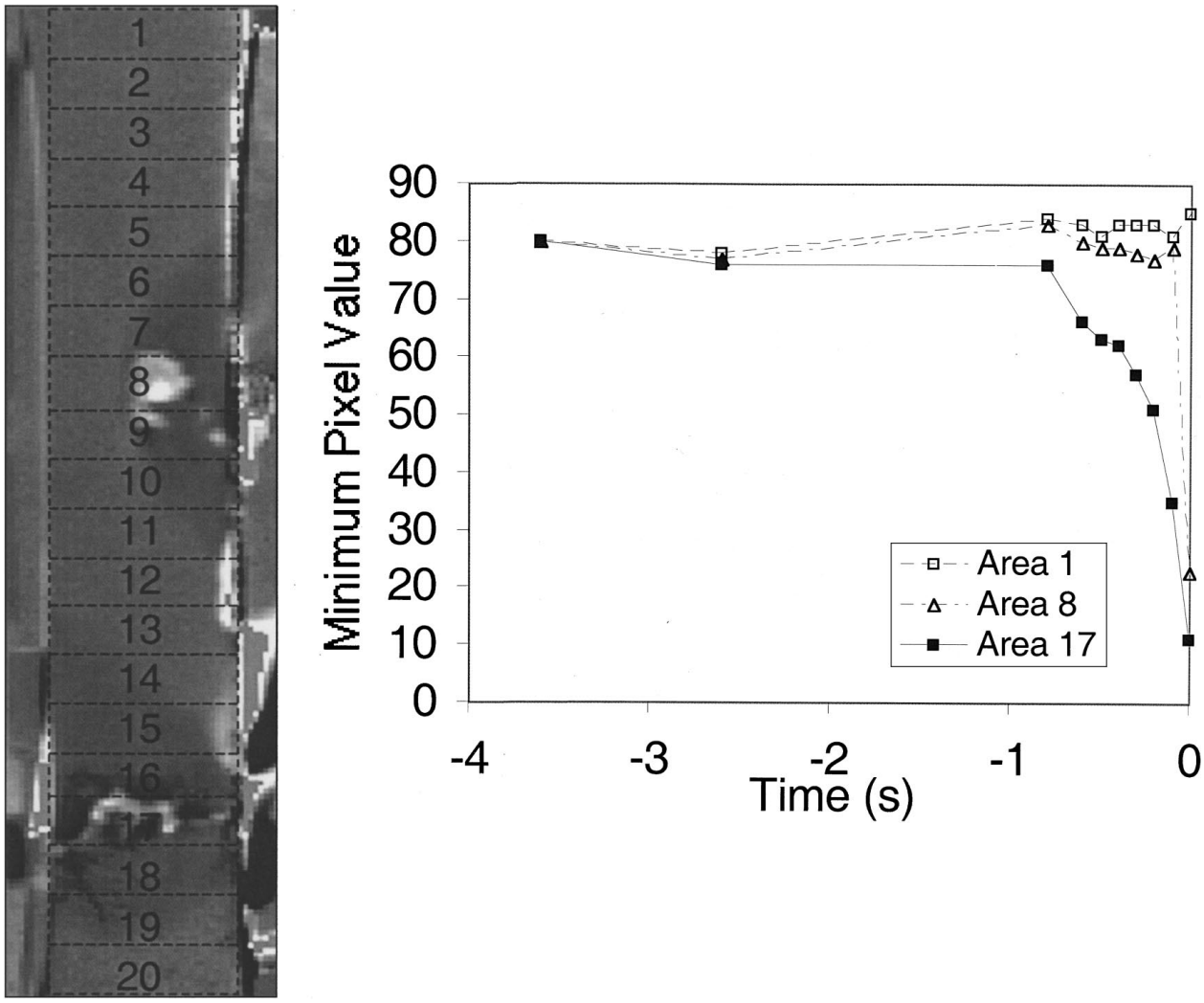


*Figure 11* The digital image can be discretized and have each segment's pixel intensity examined. Here, Area 17 shows a drop in its pixel intensity that is illustrative of the spallation even while Area 1's intensity does not change because no spallation is occurring there. This analysis can be used to quantify the spallation event and its development.

the debonding process for this spalled portion initiated in the back side of the specimen away from the camera's field of view.

To further quantify the spallation event and its associated surface temperature changes, each processed image was divided into 20 regions along the length of the specimen (Fig. 11). The minimum and maximum pixel values for each region were determined as a function of time. The minimum pixel value was favored in this particular analysis because increased debonding lowers the temperature in the region of interest. The graph in Fig. 11 illustrates the minimum pixel value as a function of time prior to spallation for Regions 1, 8, and 17. The data for Region 17, which is associated with Spalled Region 2, clearly showed that debonding started approximately 1 second prior to spallation in the IR camera's field of view.

One primary advantage of the described IR monitoring technique is that it could detect coating debonding. The debonded regions, which appeared as darker shades of gray, were not visible under normal optical imaging. Consequently the IR imaging method has a number of applications associated with the study of TBCs. For example, by extending the method to the real-time analysis of IR images, one may purposely interrupt mechanical testing so that the debonded region can be further analyzed using other non-destructive characterization methods such as piezospectroscopy. The image analysis technique could also be applied to the evaluation of coated components such as turbine blades before and after engine testing. The detection of subsurface damage would of course require that one establish controlled thermal gradients through the thickness of the coated component.

## 4. Summary

The combined use of high-resolution infrared imaging and controlled mechanical testing of TBCs is a very effective method to characterize TBC failure. Infrared imaging was used to identify and track TBC damage evolution because surface-temperature changes were a function of the damage. Mechanical testing provided a link to the identified spallation event because it identified the associated compressive strain to failure.

The potential of this coupled use of controlled mechanical testing and infrared imaging with controlled thermal gradient imposition is quite large as they may

be used in tandem to characterize the mechanical deformation of any specimen, material, or component whose surface temperature changes as a consequence of surface or even volumetric deformation.

## References


1. J. A. HAYNES, M. K. FERBER, W. D. PORTER and E. D. RIGNEY, "Isothermal and Cyclic Oxidation of an Air Plasma-Sprayed Thermal Barrier Coating," ASME Publication 96-GT-286 (1996).
2. R. B. DINWIDDIE, S. C. BEECHER, Q. D. PORTER and B. A. NAGARAZ, IGTI Publication 96-GT-282, ASME, New York, New York, 1996.
3. J. T. DEMASI, K. D. SHEFFLER and M. ORTIZ, United Technologies Corporation, NASA Contractor Report 182230, December 1989.
4. S. M. MEIER, D. M. NISSLEY and K. D. SHEFFLER, United Technologies Corporation, NASA Contractor Report 189111, July 1991.
5. R. V. HILLERY, B. H. PILSNER, R. L. MCKNIGHT, T. S. COOK and M. S. HARTLE, General Electric Corporation, NASA Contractor Report 180807, November 1988.
6. T. A. CRUSE, S. E. STEWART and M. ORTIZ, *J. Eng. for Gas Turbines and Power* **110**(10) (1998) 610.
7. J. A. HAYNES, M. K. FERBER, W. D. PORTER and E. D. RIGNEY, *Oxidation of Metals* **52**[1–2] (1999) 31–76.
8. D. W. JORDON and K. T. FABER, *Thin Solid Films* **235** (1993) 137.
9. A. G. EVANS and J. W. HUTCHINSON, *J. Solids Struct.* **20** (1984) 455.
10. J. A. HAYNES, E. D. RIGNEY, M. K. FERBER and W. D. PORTER, *Surface and Coatings Technology* **86/87** (1996) 102.
11. M. J. LANCE, J. A. HAYNES, W. R. CANNON and M. K. FERBER, "Piezospectroscopic Characterization of Thermal Barrier Coatings," in preparation.
12. R. A. MILLER, *J. Eng. for Gas Turbines and Power*, **111**(5) (1989) 301.
13. S. M. MEIER, D. M. NISSLEY, K. D. SHEFFLER and T. A. CRUSE, *ibid.* **114**(4) (1992) 258.
14. J. T. DEMASI-MARCIN, K. D. SHEFFLER and S. BOSE, *ibid.* **112**(9) (1990) 521.
15. M. ALAYA and G. GRATHWOHL, in "Materials for Advanced Power Engineering, Part II," edited by D. Coutsouradis *et al.* (Kluwer Academic, Netherlands, 1994). p. 1323.
16. M. M. NAGEL and W. T. EVANS, *J. Matls. Sci.* **28** (1993) 6247.
17. A. A. WERESZCZAK, J. G. HEMRICK, T. P. KIRKLAND, J. A. HAYNES, T. J. FITZGERALD and J. E. JUNKIN, ASME Paper No. 98-GT-403, International Gas Turbine and Aeroengine Congress & Exhibition, Stockholm, Sweden, 1998.
18. T. A. CRUSE, B. P. JOHNSON and A. NAGY, in Proceedings of the Thermal Barrier Coating Workshop, NASA Conference Publication 3312, 1995, p. 169.
19. M. K. FERBER, H-T LIN, M. J. LANCE and J. A. HAYNES, presented at the 100th Annual Meeting of the American Ceramic Society.



*Received 27 August*
*and accepted 28 October 1999*